Contents lists available at ScienceDirect

Journal of Alloys and Compounds

journal homepage: www.elsevier.com/locate/jallcom

A Ni-free Zr-based bulk metallic glass with remarkable plasticity

Jason S.C. Jang[a,*], K.C. Wu[b], S.R. Jian[b], P.J. Hsieh[b], J.C. Huang[c], C.T. Liu[d]

[a] Department of Mechanical Engineering, Institute of Materials Science and Engineering, National Central University, Chung-Li, 32001, Taiwan, ROC
[b] Department of Materials Science and Engineering, I-Shou University, Kaohsiung, 840, Taiwan, ROC
[c] Department of Materials and Optoelectronic Science, Center for Nanoscience and Nanotechnology, National Sun Yat-Sen University, Kaohsiung, 804, Taiwan, ROC
[d] Department of Mechanical Engineering, The Hong Kong Polytechnic University, Hong Kong

ARTICLE INFO

ABSTRACT

The effect of Nb and Pd combination on the glass forming ability (GFA) and mechanical properties of $Zr_{53}Cu_{30}Nb_xPd_{9-x}Al_8$ ($x = 3.5$–6.0) bulk metallic glasses (BMGs) were systematically investigated by X-ray diffractometry (XRD), differential scanning calorimetry (DSC), transmission electron microscopy (TEM), and compression test. TEM observation revealed that a nanocrystalline phase embeds in the amorphous matrix of the as-cast $Zr_{53}Cu_{30}Nb_{4.5}Pd_{4.5}Al_8$ alloy. A tiny nano-crystalline phase (with size about 5–20 nm) embedded uniformly in the amorphous matrix of the $Zr_{53}Cu_{30}Nb_{4.5}Pd_{4.5}Al_8$ alloy was observed and identified to be the tetragonal structured $NbPd_3$ phase based on the analyses of nano beam electron diffraction. According to the results of thermal analyses, the composition of $Zr_{53}Cu_{30}Nb_5Pd_4Al_8$ and $Zr_{53}Cu_{30}Nb_{4.5}Pd_{4.5}Al_8$ present the optimum GFA as well as thermal stability in the $Zr_{53}Cu_{30}Nb_xPd_{9-x}Al_8$ ($x = 3.5$–6.0) alloy system. In addition, the result of compression test shows that the yield strength significantly increases from 1700 MPa ($Zr_{53}Cu_{30}Nb_5Pd_4Al_8$) to 1900 MPa ($Zr_{53}Cu_{30}Nb_{4.5}Pd_{4.5}Al_8$). A remarkable compression plastic strain (11.2%) occurs at $Zr_{53}Cu_{30}Nb_{4.5}Pd_{4.5}Al_8$ BMG rod with 2 mm in diameter. This significant increase in plasticity is presumably due to the restriction on shear banding by the nano-size second phase.

© 2011 Elsevier B.V. All rights reserved.

1. Introduction

Based on the combination of high elastic strain limit (∼2%), high strength (∼2 GPa), relatively elastic modulus (60–100 GPa), good wear resistance, good biocompatibility, exceptional glass-forming ability (GFA) for casting a precision net-shape component with near perfect as-cast surfaces, and an extremely wide super cooled liquid region (ΔT_x is above 50 K, ΔT_x is defined as the difference between the glass transition temperature T_g and the onset crystallization temperature T_x), Zr-based bulk metallic glasses (BMGs) are considered to be one of the most promising biomedical materials [1–7]. However, most Zr-based BMGs contain Ni as an important constituent to maintain its high GFA. Since Ni-bearing alloys are usually blamed for the occurrence of Ni-contact allergy, the existence of Ni constituent has seriously limited the biomedical application of Zr-based BMGs. Accordingly, a Ni-free Zr–Fe–Al–Cu BMG alloy system was first reported by Jin and Loeffler [8], which shows excellent GFA and satisfactory biocompatibility [9]. More recently, Qiu et al. has also developed one Ni-free $Zr_{60}Nb_5Cu_{22.5}Pd_5Al_{7.5}$ by substituting

the Ni with Pd and Nb [6,10]. This BMG exhibits quite good mechanical properties, good corrosion resistance in an artificial body fluid, and reasonably good biocompatibility. However, there is no systematic investigation about the combination effect of Pd and Nb on the GFA and mechanical properties of these Ni-free Zr-based BMGs.

In the present study, a high GFA $Zr_{53}Cu_{30}Ni_9Al_8$ alloy which computationally designed by thermodynamics and deep eutectic methodology [11–13] is selected as the base alloy for studying the combination effect of Pd and Nb on the GFA, thermal stability, and mechanical properties of the Ni-free Zr-based BMG alloy system.

2. Experimental procedure

The alloy ingots based on the compositions of $Zr_{53}Cu_{30}Nb_xPd_{9-x}Al_8$ alloy ($x = 2.5$–6.5) by atomic percentage were firstly prepared by arc melting of the appropriate mixture of pure elements, including Zr (99.8 wt.% purity), Ni (99.9 wt.% purity), Cu (99.99 wt.% purity), Al (99.99 wt.% purity), and Si (99.99% purity), under a Ti-gettered argon atmosphere. Then the alloy ingots were remelted in an arc furnace under a purified argon atmosphere. After complete melting, the liquid alloy was suction cast into the water-cooled Cu mold to form alloy rods with diameter of 2–4 mm. The differential scanning calorimetry (DSC) with a heating rate of 20 K/min, X-ray diffraction (XRD, Scintag X-400 X-ray diffractometer, Cu-Kα radiation) and transmission electron microscopy (TEM, Philip, Tecnai G2 at 200 keV) are used to ascertain

* Corresponding author. Tel.: +886 3 4267379; fax: +886 3 4254501.
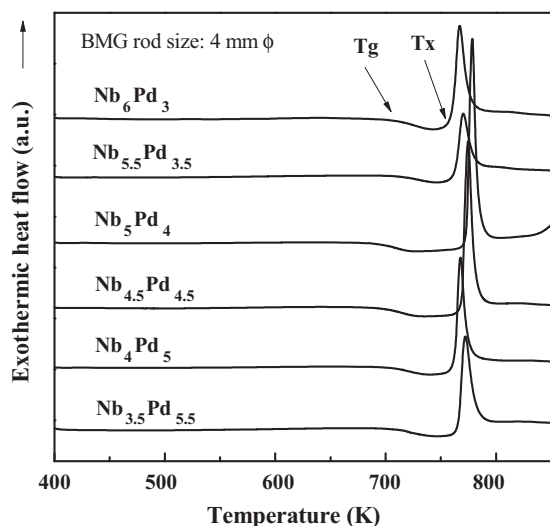E-mail address: jscjang@ncu.edu.tw (J.S.C. Jang).

Fig. 1. DSC plots of $Zr_{53}Cu_{30}Nb_xPd_{9-x}Al_8$ alloy ($x=2.5$–6.5) alloy rods with 4 mm in diameter by a heating rate of 20 K/min.

the amorphous nature of the as-cast alloys. Heating rates of 10–60 K/min were selected for the non-isothermal DSC analysis to reveal the crystallization behavior. Several temperatures between T_g and T_x were selected for the isothermal DSC analysis to study the crystallization kinetics. The hardness was examined by using Akashi MVK-H11 micro hardness tester. The rod specimens with an aspect ratio of 2:1 (height/diameter) are tested in compression under an initial strain rate of $2 \times 10^{-4}\,s^{-1}$ at room temperature by using a MTS 810 universal testing machine. Both ends of the specimens are polished to make them parallel to each other prior to the compression test. Multiple compression tests were conducted for confirming the reproducible trend and the scattering of the stress and strain was less than ±5% (i.e., less than ±100 MPa for engineering stresses and less than ±0.5% for engineering strains, respectively). The fracture surfaces of the deformed specimens are examined by scanning electron microscopy (SEM, Hitachi S4700 FESEM).

3. Results and discussions

3.1. Thermal properties of the as-cast Zr-based BMG rods

The DSC scans of the $Zr_{53}Cu_{30}Nb_xPd_{9-x}Al_8$ alloy rods with diameter of 4 mm are shown in Fig. 1. All of the samples exhibit a clear glass transition followed by a supercooled liquid region and then exothermic reaction due to crystallization. In addition, the lowest liquidus temperature (about 1176 K) occurs at the $Zr_{53}Cu_{30}Nb_5Pd_4Al_8$ alloy, as shown in Table 1. This implies that the $Zr_{53}Cu_{30}Nb_5Pd_4Al_8$ alloy would posses the highest glass forming ability in this $Zr_{53}Cu_{30}Nb_xPd_{9-x}Al_8$ alloy system according to the deep eutectic theory of Turnbull [14]. Other popular measures of the GFA are γ ($\gamma = T_x/T_g + T_l$) [15] and (γ_m ($\gamma_m = (2T_x - T_g)/T_l$) [16], which exhibit irregular trend for the studied alloy system and their different combinations of Nb and Pd additions. The measures of γ and γ_m have been reported to be more accurate than T_{rg} ($T_{rg} = T_g/T_l$) for multiple component BMGs [17]. Based on the results of γ and γ_m, it has therefore been found that the optimum GFA occurs at the composition of $Zr_{53}Cu_{30}Nb_5Pd_4Al_8$ and $Zr_{53}Cu_{30}Nb_{4.5}Pd_{4.5}Al_8$.
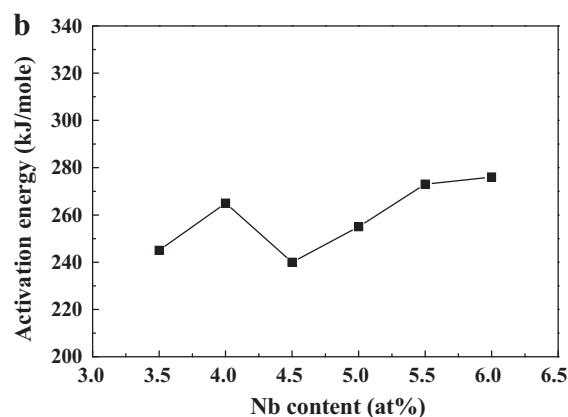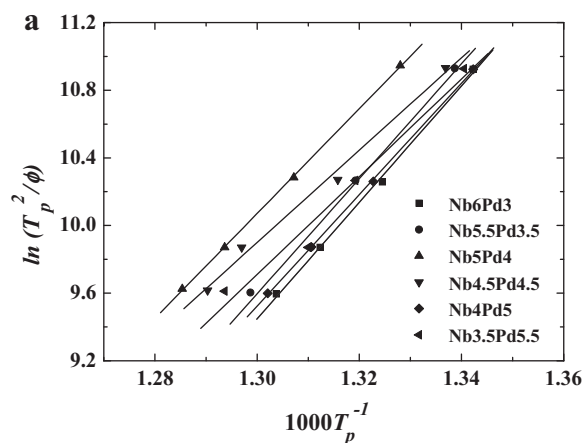

Fig. 2. (a) Kissinger plots of the DSC peaks for crystallization of $Zr_{53}Cu_{30}Nb_xPd_{9-x}Al_8$ alloys, (b) the activation energy estimated by Kissinger plots as a function of Nb content for $Zr_{53}Cu_{30}Nb_xPd_{9-x}Al_8$ amorphous alloys.

The activation energy of crystallization for the $Zr_{53}Cu_{30}Nb_xPd_{9-x}Al_8$ alloys was determined by means of the Kissinger plot [18]

$$\ln \frac{b}{T^2} = -\frac{E_a}{RT_p} + \text{constant} \tag{1}$$

where b is the heating rate, T_p is peak temperature of crystallization, R is the gas constant, and E_a is the activation energy. The activation energy of crystallization can be determined from the slope of a plot of the $\ln(b/T_p^2)$ against $1/T_p$. The $\ln(b/T_p^2)$ as a function of $1/T_p$ is plotted in Fig. 2(a). Fig. 2(b) shows the activation energy of crystallization calculated by Kissinger plot as a function of Nb content for $Zr_{53}Cu_{30}Nb_xPd_{9-x}Al_8$ alloys. All of the activation energy of these $Zr_{53}Cu_{30}Nb_xPd_{9-x}Al_8$ alloys locates around 240–275 kJ/mole and does not present any regulation with the combination additions of Nb and Pd.

By using the Johnson–Mehl–Avrami (JMA) isothermal analysis for volume fraction x transformed as a function of time t based on

Table 1
Thermal parameters of the $Zr_{53}Cu_{30}Nb_xPd_{9-x}Al_8$ alloy ($x=2.5$–6.5) alloys obtained from DSC analysis.

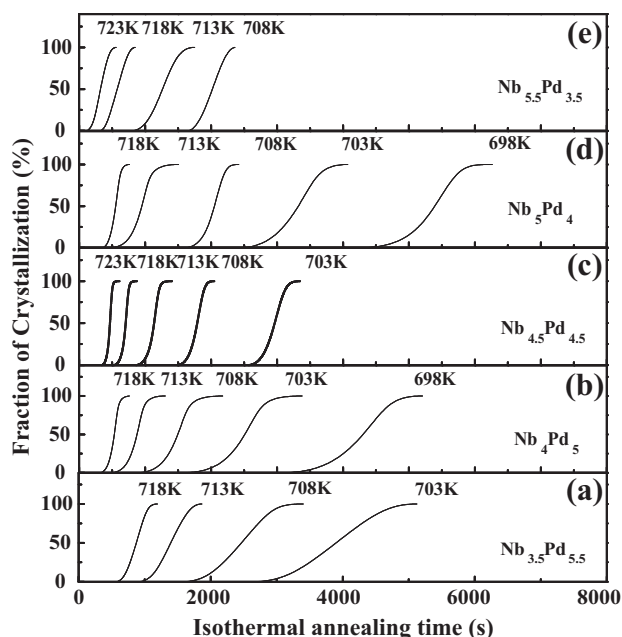|	T_g (K)	T_x (K)	ΔT_x (K)	T_l (K)	T_{rg}	γ	γ_μ
Nb_6Pd_3	689	748	59	1209	0.570	0.394	0.667
$Nb_{5.5}Pd_{3.5}$	695	753	58	1188	0.585	0.400	0.683
Nb_5Pd_4	692	758	66	1176	0.588	0.406	0.700
$Nb_{4.5}Pd_{4.5}$	690	758	68	1178	0.586	0.406	0.701
Nb_4Pd_5	698	753	55	1188	0.587	0.399	0.680
$Nb_{3.5}Pd_{5.5}$	697	754	57	1181	0.590	0.401	0.687

Fig. 3. Crystallization fraction as a function of annealing time within the supercooled liquid temperature region for $Zr_{53}Cu_{30}Nb_xPd_{9-x}Al_8$ alloy ($x = 2.5–6.5$) amorphous alloys.

the following Eq. (2):

$$x(t) = 1 - \exp[-(kt)^n] \qquad (2)$$

$Zr_{53}Cu_{30}Nb_xPd_{9-x}Al_8$ amorphous alloys were annealed isothermally at several temperatures between T_g and T_x. To construct the JMA plots, the volume fraction of crystallization at time t was assumed to be the same as that of heat released. Therefore, the crystallization fraction, x, which obtained by measuring the partial area under the DSC peak up to time t as a function of annealing time is plotted as shown in Fig. 3. In addition, the incubation time as a function of isothermal annealing temperature exhibits a similar decreasing trend for the entire $Zr_{53}Cu_{30}Nb_xPd_{9-x}Al_8$ alloys as shown in Fig. 4. Only the $Zr_{53}Cu_{30}Nb_5Pd_4Al_8$ and $Zr_{53}Cu_{30}Nb_{4.5}Pd_{4.5}Al_8$ alloys present slightly better thermal stability. Since the atomic radius of Nb (0.146 nm) Pd (0.137 nm) [19] is just between the atomic group of Zr (0.160 nm) and Cu (0.128 nm), that the combination additions of Nb and Pd, which substitute the Ni constitute (0.125 nm), would increase the packing density of the base alloy. In addition, both of the Zr–Pd (−91 kJ/mole) and
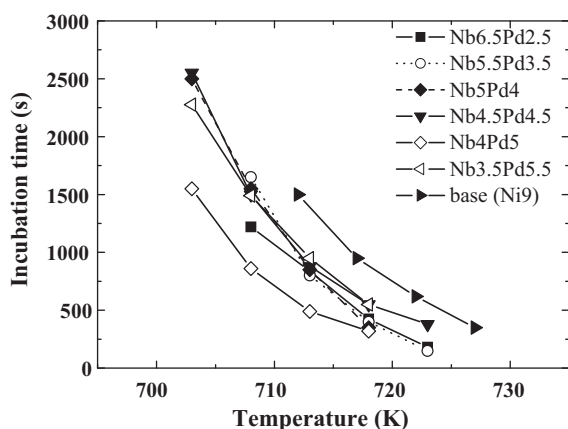

Fig. 4. Incubation time as a function of isothermal annealing temperature for $Zr_{53}Cu_{30}Nb_xPd_{9-x}Al_8$ alloy ($x = 2.5–6.5$) amorphous alloys.
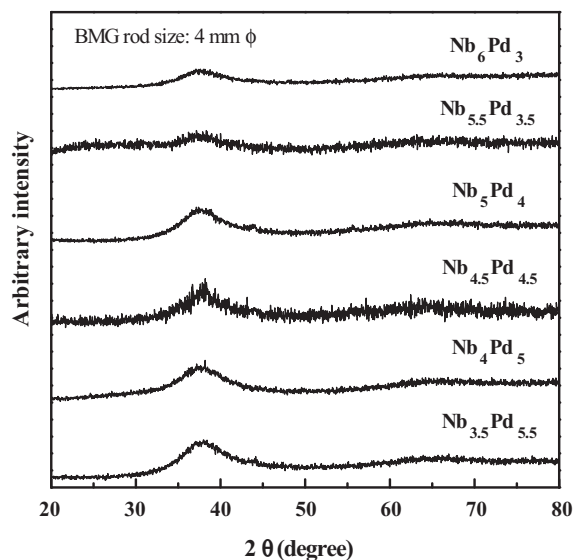

Fig. 5. (a) X-ray diffraction patterns of the as-cast $Zr_{53}Cu_{30}Nb_xPd_{9-x}Al_8$ alloy ($x = 2.5–6.5$) amorphous alloy rods with 4 mm in diameter.

Cu–Pd (−14 kJ/mole) [20] binary system has a large negative heat of mixing which can form strong atomic bonding of Zr–Pd and Cu–Pd atomic pairs. On the other hand, the other two binary systems, Zr–Nb (+4 kJ/mole) and Cu–Nb (+3 kJ/mole) [20] present a small positive heat of mixing which may results in deteriorating the strong atomic bonding configuration. Therefore, the total effect of topological packing and atomic bonding of the combination additions of Nb and Pd on thermal stability for the base alloy is suggested to be compensated each other and exhibits slight decrease in thermal stability finally.

3.2. Microstructure of the as-cast Zr-based BMG rods

Fig. 5 shows the X-ray diffraction (XRD) patterns obtained from the $Zr_{53}Cu_{30}Nb_xPd_{9-x}Al_8$ alloy rods with 4 mm in diameter. The diffraction patterns of these $Zr_{53}Cu_{30}Nb_xPd_{9-x}Al_8$ alloy rods all exhibits a broad maximum 2θ around $40°$. However, the XRD data does not allow any conclusion about a possible presence of a small volume fraction crystalline phase in the material. Therefore TEM analysis was done to investigate the microstructure more detail. A tiny nano-crystalline phase (with size about 5–20 nm) embedded uniformly in the amorphous matrix for the $Zr_{53}Cu_{30}Nb_{4.5}Pd_{4.5}Al_8$ alloy was revealed by TEM observation, as illustrated in Fig. 6(a). In addition, it was found that most of these nanocrystals have the size (D) less than 10 nm and the interparticle spacing (l) is about 30 nm. If we use the equation of $C_v = D/l^2$, the calculated volume fraction of the crystals is about 1.1%, which, given the size of the crystals, is very unlikely to contribute to any signal in the shown XRD spectra. Based on the analyses of nano beam electron diffraction as shown in Fig. 6(b–d), the d-spacing of these nano particles relatively matches with that of the tetragonal structured $NbPd_3$ phase. The formation of $NbPd_3$ phase is suggested due to the very large negative heat of mixing (−53 kJ/mole) of Nb–Pd binary system, which may favorable to form intermetallic compound during solidification.

3.3. Mechanical performance

According to the results of hardness test for these $Zr_{53}Cu_{30}Nb_xPd_{9-x}Al_8$ BMG rods, a small increase in macro hardness was revealed when the Pd content exceed 4.5 at.% of these BMGs. All of the hardness is within 490–520 Hv as shown in Fig. 7. However, the result of compression test exhibits different
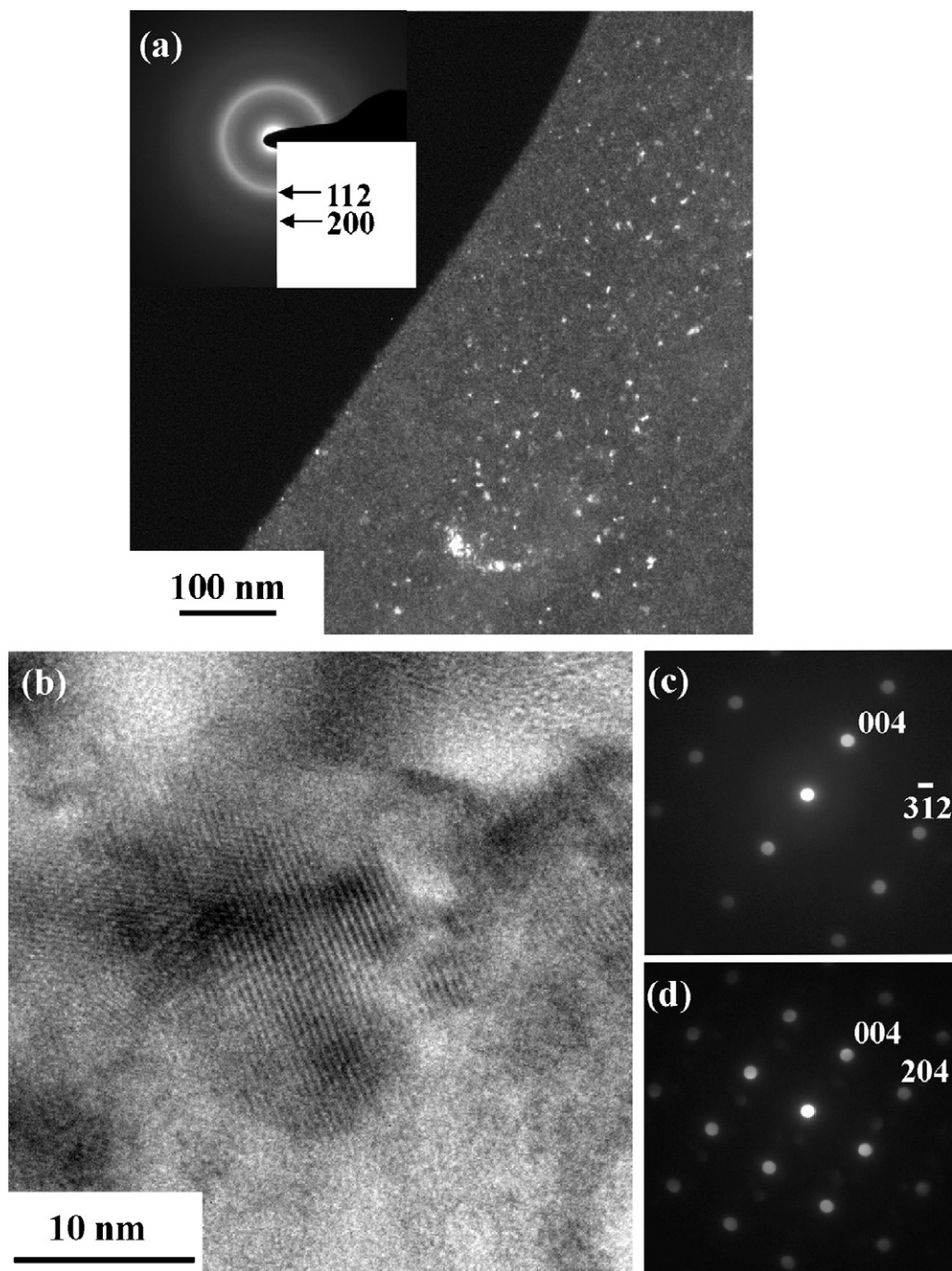
Fig. 6. TEM images and electron diffraction patterns of the as-quenched $Zr_{53}Cu_{30}Nb_{4.5}Pd_{94.5}Al_8$ alloy, (a) dark filed TEM image of nanocrystalline phase which reflected from the inner ring of the insert selected area diffraction pattern, (b) high resolution TEM image, (c) nano beam electron diffraction pattern of $NbPd_3$ phase with B [1 3 0], and (d) nano beam electron diffraction pattern of $NbPd_3$ phase with B [0 1 0].

trend of yield strength from the hardness test, the yield strength significantly increases from 1700 MPa $(Zr_{53}Cu_{30}Nb_5Pd_4Al_8)$ to 1900 MPa $(Zr_{53}Cu_{30}Nb_{4.5}Pd_{4.5}Al_8)$ as shown in Fig. 8. A remarkable compression plastic strain (11.2%) occurs at $Zr_{53}Cu_{30}Nb_{4.5}Pd_{4.5}Al_8$ BMG rod with 2 mm in diameter. This significant increase in plasticity is presumably due to the restriction on shear banding by the nano-size second phase. It has been reported that the formation of nano-sized second phase, either in situ precipitation [21–24] or phase separation [25–30], is an effective approach to enhance the plasticity of BMG. Similar to the composite materials, the structural heterogeneities in the amorphous phase can act

as both initiation sites for shear bands as well as obstacles to shear band propagation. This leads to form multiple shear bands, and consequently results in improving of the total plasticity. Schuh et al. [31] also suggest that nanocrystals may slightly enhance shear band initiation and increased plastic strain in compression.

The extent of plastic deformation in BMGs is quite dependent on the density of shear band. Therefore, it was expected that the two specimens, $Zr_{53}Cu_{30}Nb_{4.5}Pd_{4.5}Al_8$ and $Zr_{53}Cu_{30}Nb_5Pd_4Al_8$ BMGs, would differ in their density and morphology of shear bands. From the SEM images (which taken from the side surfaces near the
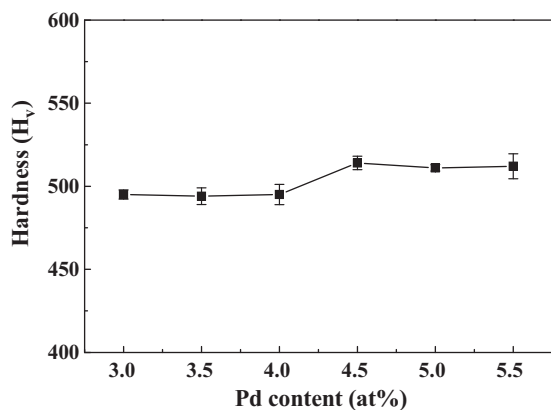
Fig. 7. Hardness as a function of Nb addition for $Zr_{53}Cu_{30}Nb_xPd_{9-x}Al_8$ BMG rods with diameter of 2 mm.

Fig. 8. Compression stress–strain curves of the $Zr_{53}Cu_{30}Nb_xPd_{9-x}Al_8$ BMG rods with diameter of 2 mm.

fracture area) shown in Fig. 9(a and b), different shear band morphologies can be observed. In addition, the fracture surface of the $Zr_{53}Cu_{30}Nb_{4.5}Pd_{4.5}Al_8$ BMG specimen reveals a mixed morphology, consisting of vein-like pattern and highly rough regions, as shown in Fig. 9(c). The mixture of vein and rough regions is much differ from the flat vein-like pattern, which is the main part of the compressive fracture surfaces for most monolithic BMGs and the $Zr_{53}Cu_{30}Nb_5Pd_4Al_8$ BMG sample (as shown in Fig. 9(d)). In addition, the highly rough region of fracture surface indicates that the shear bands are highly branched and their movement is rather wavy in nature, implies that there exists strong interaction between shear bands and the nano-precipitates. It was reported that the shear band formation can be suppressed by nanocrystalline particles with a band-like arrangement [32]. This would result in the formation of multip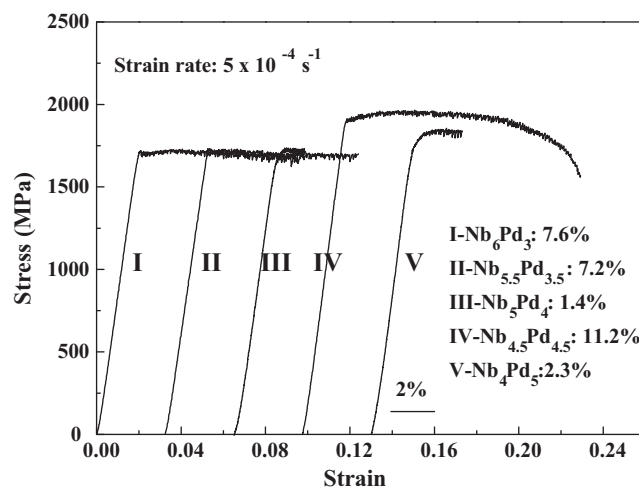le shear bands and decrease the stress concentration for further propagation of shear band, and so as to significantly improve their plasticity.

4. Conclusion

Based on the results of thermal analyses, X-ray diffraction, and SEM and TEM observation for the $Zr_{53}Cu_{30}Nb_xPd_{9-x}Al_8$ ($x = 3.5$–5.5) amorphous alloys, the combination effect of Nb and Pd on the thermal and mechanical properties can be summarized as follows:

(1) The value of GFA index, γ and γ_m all exhibit irregular trend with the combination of Nb and Pd additions. The optimum GFA was
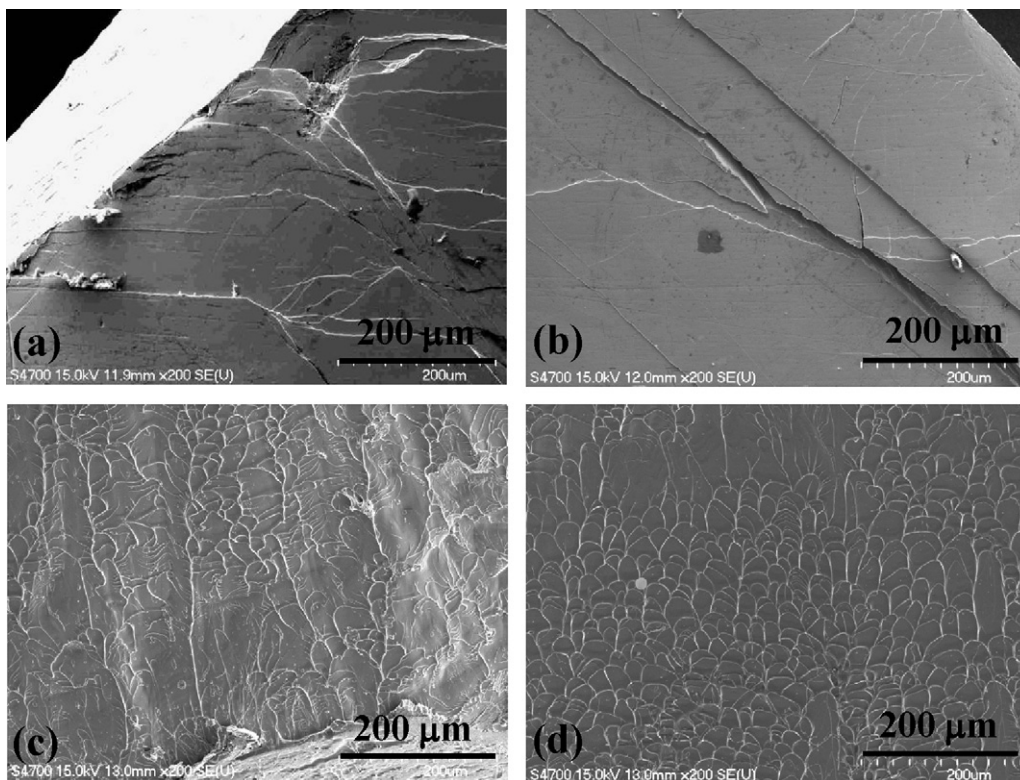

Fig. 9. SEM images of the specimen surface near the fracture area for (a) $Zr_{53}Cu_{30}Nb_{4.5}Pd_{4.5}Al_8$ and (b) $Zr_{53}Cu_{30}Nb_5Pd_4Al_8$ BMG rods; SEM images of different type vein pattern at some area of the fracture surface for (c) $Zr_{53}Cu_{30}Nb_{4.5}Pd_{4.5}Al_8$ and (d) $Zr_{53}Cu_{30}Nb_5Pd_4Al_8$ BMG rods with diameter of 2 mm after compression test.

found to occur at the composition of $Zr_{53}Cu_{30}Nb_5Pd_4Al_8$ and $Zr_{53}Cu_{30}Nb_{4.5}Pd_{4.5}Al_8$.

(2) $Zr_{53}Cu_{30}Nb_5Pd_4Al_8$ and $Zr_{53}Cu_{30}Nb_{4.5}Pd_{4.5}Al_8$ alloys present slightly better thermal stability. However, the total effect of topological packing and atomic bonding of the combination additions of Nb and Pd on thermal stability of the base alloy is suggested to be compensated each other and exhibits slight decrease in thermal stability than the base alloy finally.

(3) TEM observation revealed that a nanocrystalline phase co-existing in the amorphous matrix of the as-cast $Zr_{53}Cu_{30}Nb_{4.5}Pd_{4.5}Al_8$ alloy. One tiny nano-crystalline phase (with size about 5–20 nm) embedded uniformly in the amorphous matrix of the $Zr_{53}Cu_{30}Nb_{4.5}Pd_{4.5}Al_8$ alloy was observed and was identified to be the tetragonal structured $NbPd_3$ phase according to the analyses of nano beam electron diffraction.

(4) The result of compression test shows that the yield strength significantly increases from 1700 MPa ($Zr_{53}Cu_{30}Nb_5Pd_4Al_8$) to 1900 MPa ($Zr_{53}Cu_{30}Nb_{4.5}Pd_{4.5}Al_8$). Moreover, a remarkable compression plastic strain (11.2%) occurs at $Zr_{53}Cu_{30}Nb_{4.5}Pd_{4.5}Al_8$ BMG rod with 2 mm in diameter. This significant increase in plasticity is presumably due to the restriction on shear banding by the nano-size second phase. This would result in the formation of multiple shear bands and decrease the stress concentration for further propagation of shear band, and so as to significantly improve their plasticity.

Acknowledgements

References

[1] A. Inoue, B.L. Shen, H. Koshiba, H. Kato, A.R. Yavari, Nat. Mater. 2 (2003) 663.
[2] W.L. Johnson, MRS Bull. 24 (1999) 42.
[3] A. Inoue, Acta Mater. 48 (2000) 279.
[4] J. Schroers, N. Paton, Adv. Mater. Proc. 164 (2006) 61.
[5] C.J. Gilbert, V. Schroeder, R.O. Ritchie, Metall. Mater. Trans. A 30 (1999) 1739.
[6] C.L. Qiu, Q. Chen, L. Lu, K.C. Chan, J.X. Zhou, P.P. Chen, S.M. Zhang, Scripta Mater. 55 (2008) 605.
[7] C.A. Schuh, T.C. Hufnagel, U. Ramamurty, Acta Mater. 55 (2007) 4067.
[8] K. Jin, J.F. Loeffler, Appl. Phys. Lett. 86 (2005) 241909.
[9] S. Buzzi, K.F. Jin, P.J. Uggowitzer, S. Tosatti, I. Gerber, J.F. Loeffler, Intermetallics 14 (2006) 729.
[10] L. Liu, C.L. Qiu, C.Y. Huang, Y. Yu, H. Huang, S.M. Zhang, Intermetallics 17 (2009) 235.
[11] Z.P. Lu, J. Shen, D.W. Xing, J.F. Sun, C.T. Liu, Appl. Phys. Lett. 89 (2006) 071910.
[12] J.S.C. Jang, S.R. Jian, C.F. Chang, L.J. Chang, Y.C. Huang, T.H. Li, J.C. Huang, C.T. Liu, J. Alloys Compd. 478 (2009) 215.
[13] J.S.C. Jang, C.F. Chang, Y.C. Huang, J.C. Huang, W.J. Chiang, C.T. Liu, Intermetallics 17 (2009) 200.
[14] D. Turnbull, Contemp. Phys. 10 (1969) 473.
[15] Z.P. Lu, C.T. Liu, Intermetallics 12 (2004) 1035.
[16] X.H. Du, J.C. Huang, C.T. Liu, Z.P. Lu, Jpn. J. Appl. Phys. 101 (2007) 086108.
[17] S. Guo, Z.P. Lu, C.T. Liu, Intermetallics 18 (2010) 883.
[18] H.E. Kissinger, Analyst. Chem. 29 (1957) 1702.
[19] The periodic table of elements, http://library.thinkquest.org/12909/main2.html.
[20] F.R. Boer, Cohesion in Metals, North Holland (Elsevier Sci. Pub. Co.), New York, USA, 1988.
[21] J. Das, M.B. Tang, K.B. Kim, R. Theissmann, F. Baier, W.H. Wang, J. Eckert, Phys. Rev. Lett. 94 (2005) 205501.
[22] K.B. Kim, J. Das, F. Baier, M.B. Tang, W.H. Wang, J. Eckert, Appl. Phys. Lett. 88 (2006) 051911.
[23] W. Dong, H. Zhang, J. Cai, W. Sun, A. Wang, H. Li, Z. Hu, J. Alloys Compd. 425 (2006) L1.
[24] Z. Zhang, F. Wu, G. He, J. Eckert, J. Mater. Sci. Technol. 23 (2007) 747.
[25] J.C. Oh, T. Ohkubo, Y.C. Kim, E. Fleury, K. Hono, Scripta Mater. 53 (2005) 165.
[26] K.B. Kim, J. Das, X.D. Wang, X. Zhang, J. Eckert, S. Yi, Philos. Mag. Lett. 86 (2006) 479.
[27] K.F. Yao, F. Ruan, Y.Q. Yang, N. Chen, Appl. Phys. Lett. 88 (2006) 122106.
[28] X.H. Du, J.C. Huang, K.C. Hsieh, Y.H. Lai, H.M. Chen, J.S.C. Jang, P.K. Liaw, Appl. Phys. Lett. 91 (2007) 131901.
[29] E.S. Park, J.S. Kyeong, D.H. Kim, Scri. Mater. 57 (2007) 49.
[30] X.H. Du, J.C. Huang, H.M. Chen, H.S. Chou, Y.H. Lai, K.C. Hsieh, J.S.C. Jang, P.K. Liaw, Intermetallics 17 (2009) 607.
[31] C.A. Schuh, T. Hufnagel, U. Ramamurty, Acta Mater. 55 (2007) 4067.
[32] J. Saida, A.D.H. Setyawan, H. Kato, A. Inoue, Appl. Phys. Lett. 87 (2005) 151907.